Influence of magnetic-field-induced tuning of disorder and band structure on the magnetoresistance of paramagnetic dilute magnetic semiconductors

C. Michel, P. J. Klar,* S. D. Baranovskii, and P. Thomas
Department of Physics and Material Sciences Center, Philipps University, Renthof 5, 35032 Marburg, Germany
(Received 1 October 2003; published 27 April 2004)

We study theoretically the magnetotransport in *p*-type wide-gap dilute magnetic semiconductors in the paramagnetic phase. Two models (referred to as mobility model and network model) based on a minimal description of the valence-band structure and the acceptor state of the dilute magnetic semiconductors are discussed. In both models, band filling effects, magnetic-field splitting of the band states due to the *p-d* exchange interaction, as well as effects of magnetic-field independent disorder are included whereas carrier-carrier interactions other than those responsible for the local magnetism of the Mn ions are neglected. Despite the exclusion of many-body effects in the bands, positive as well as negative magnetoresistance effects are predicted which show a qualitative agreement with recent experiments on *p*-type dilute magnetic semiconductors [Ye *et al.*, J. Supercond. **16**, 159 (2003); Nam *et al.*, *ibid.* **16**, 335 (2003)]. The differences between the two models arise from a different, model-specific weighting of disorder and occupation effects.

DOI: 10.1103/PhysRevB.69.165211 PACS number(s): 75.50.Pp, 72.20.My, 72.80.Ng

I. INTRODUCTION

Dilute magnetic semiconductors (DMS's) exhibit unusual magnetic properties due to exchange interaction between the localized spins of the magnetic ions and the spins of the free carriers. Two major classes of DMS are wide-gap (II,Mn)VI and (III,Mn)V alloys.[1–3] The magnetism of these DMS will strongly depend on the Mn content, the electronic configuration of the Mn ion, and on the degree of doping. The (II,Mn)VI compounds, where Mn is isoelectronic to the group II cations, exhibit paramagnetic behavior up to very high Mn contents. On the other hand, the (III,Mn)V compounds, where the Mn is incorporated as an acceptor, might also show a ferromagnetic phase. For example, $Ga_{1-x}Mn_xAs$ with $x \simeq 0.1$ is *p*-type and exhibits Curie temperatures as high as $T_C = 175$ K,[5] For $Ga_{1-x}Mn_xN$ even higher Curie temperatures are predicted.[6,7] The ferromagnetism is mediated by the free holes. Nevertheless, in the dilute Mn regime, GaAs:Mn shows a paramagnetic phase down to very low temperatures. (II,Mn)VI semiconductors such as $Zn_{1-x}Mn_xTe$ can be made ferromagnetic with a T_C of a few kelvin by codoping with acceptors such as N to increase the number of free holes.[8]

Both ferromagnetic and paramagnetic DMS's are currently of interest in the context of spintronics and spin optoelectronics. These technologies combine the merits of semiconductor-electronic and magnetoelectronic devices.[4] DMS's are of particular interest as spin-aligner and spin-injector materials in such devices. Possible DMS-based designs consist either of ferromagnetic DMS,[1] paramagnetic DMS,[9–12] or paramagnetic-ferromagnetic hybrid structures.[13] (Ga,Mn)As/MnAs is a typical example of such a hybrid structure. In this hybrid, ferromagnetic MnAs clusters are embedded in a paramagnetic $Ga_{1-x}Mn_xAs$ host matrix.

Several current studies show that these DMS-based hybrid systems exhibit large positive and negative magnetoresistance (MR) effects. Examples are the MR behaviors of $Ga_{1-x}Mn_xAs$/MnAs (Refs. 14–16), GaAs/ErAs (Ref. 17), GaAs:Mn/MnSb (Refs. 18 and 19) and $Ge_{1-y}Mn_y$:$Mn_{11}Ge_8$.[20] However, the microscopic mechanisms are not at all understood because the galvanomagnetic properties of such granular ferromagnetic hybrid systems depend strongly on the electronic transport properties of the paramagnetic matrix material, the magnetic properties of the clusters, and on the interaction of the electronic states of the host matrix with the ferromagnetic clusters. Of course, one essential prerequisite for understanding the galvanomagnetic properties of the hybrids are detailed experimental and theoretical studies of the transport in the paramagnetic DMS materials which act as host matrix for the clusters. In particular, theoretical models need to be developed which are extendable to the hybrid systems.

Several magnetotransport experiments were reported on wide-gap DMS alloys covering *n*-type $Cd_{1-x}Mn_xTe$ (Ref. 21) and $Cd_{1-x}Mn_xSe$, (Ref. 23) and more recently *p*-type DMS such as $Zn_{1-x}Mn_xTe$:N (Ref. 24) and paramagnetic $Ga_{1-x}Mn_xAs$.[25] It is worth noting that already the paramagnetic DMS alloy alone (i.e., without clusters) exhibits positive as well as negative MR effects.[21–25] However, these are different from those in the corresponding hybrids.[15] The unusual MR effects of the paramagnetic DMS's are explained by the interplay of band filling, magnetic-field-induced tuning of the band structure, carrier-carrier interactions, and quantum corrections.[22,26–30] An aspect, whose influence on the galvanomagnetic properties of DMS was included so far only in the magnetic polaron picture,[31] is the magnetic-field-induced tuning of the alloy disorder in these materials. It arises due to fluctuations in the Mn concentration which, in an applied magnetic field, lead to local fluctuations of the Mn-induced band splitting. Magnetic-field tuning of alloy disorder is a well-known feature of DMS.[32–35] On the other hand, it is well established that disorder in crystalline semiconductor alloys and even more in amorphous semiconductors has a considerable impact on the transport properties.[36]

Here, we discuss two models for the magnetotransport in *p*-type DMS in the paramagnetic phase: a mobility model and a network model. Both models are based on a simplified

description of the valence-band structure and the acceptor state of the DMS. Band filling effects, magnetic-field splitting of the band states due to the *p-d* exchange interaction, as well as effects of magnetic-field independent disorder are accounted for. We do not include carrier-carrier interactions other than those responsible for the local magnetism of the Mn ions. We will show that, despite the exclusion of many-body effects in the bands, positive as well as negative MR effects are predicted by the model which show a qualitative agreement with recent experiments on paramagnetic *p*-type DMS's.[24,25]

II. MODEL CALCULATIONS

A. Description of DMS

We only deal with *p*-type zinc-blende DMS. The simplified description of the band structure comprises the light hole bands (with angular momentum $j=\frac{3}{2}$ and $j_z=\pm\frac{1}{2}$) and heavy hole bands (with $j=\frac{3}{2}$ and $j_z=\pm\frac{3}{2}$) of Γ_8 symmetry. We assume that at the center of the Brillouin zone, $E_v(k=0,j_z)=0$ for all four j_z and that the Mn-acceptor level is at E_A. We assume parabolic bands for the light and heavy holes characterized by effective masses m_{lh} and m_{hh}, respectively.

In an external magnetic field H, the acceptor level E_A is not altered whereas the four valence bands exhibit the giant Zeeman splitting due to the *p-d* exchange with the Mn ions. Furthermore, we assume that the giant Zeeman splitting is independent of momentum k. The energetic positions of a valence-band state of angular momentum component j_z and momentum k varies with external field H as[2,3]

$$E_v(k,j_z,H)=E_{v0}(k,j_z)-\tfrac{1}{3}N_0\beta x_0 j_z\langle S_z\rangle, \tag{1}$$

where $E_{v0}(k,j_z=\pm\frac{1}{2})=(\hbar^2/2m_{j_z})k^2$. The effective mass is $m_{j_z}=m_{lh}$ for light holes with $j_z=\pm\frac{1}{2}$ whereas it is $m_{j_z}=m_{hh}$ for heavy holes with $j_z=\pm\frac{3}{2}$. $N_0\beta$ is the *p-d* exchange integral. x_0 is the Mn concentration and $\langle S_z\rangle$ is the z component of the $S=\frac{5}{2}$ Mn spin parallel to H in the mean-field approximation. For simplicity, for the diluted case at hand, we neglect *d-d* coupling between the Mn ions. Hence, $\langle S_z\rangle$ is given by the Brillouin function $B_{5/2}$ for $S=\frac{5}{2}$:

$$\langle S_z\rangle=\tfrac{5}{2}B_{5/2}(H,T)=\frac{5}{2}\left[\frac{6}{5}\coth\left(\frac{6\zeta}{5}\right)-\frac{1}{5}\coth\left(\frac{\zeta}{5}\right)\right], \tag{2}$$

where $\zeta=g\mu_B\mu_0 H/k_BT$. T is the temperature, $g=2$ is the g factor of the d electrons, k_B is the Boltzmann constant, and μ_B is the Bohr magneton. The resulting band-structure schemes for $H=0$ and $H\neq 0$ are illustrated in Fig. 1. We chose $|N_0\beta|=2$ eV in all calculations, typical for wide-gap (III,Mn)V and (II,Mn)VI DMS's.[1–3] We neglect effects due to Landau quantization and magnetic anisotropy in the valence band due to strain. The former is justified in the case of wide-gap DMS and the latter is a good approximation when the quantization directions due to strain and magnetic field coincide.

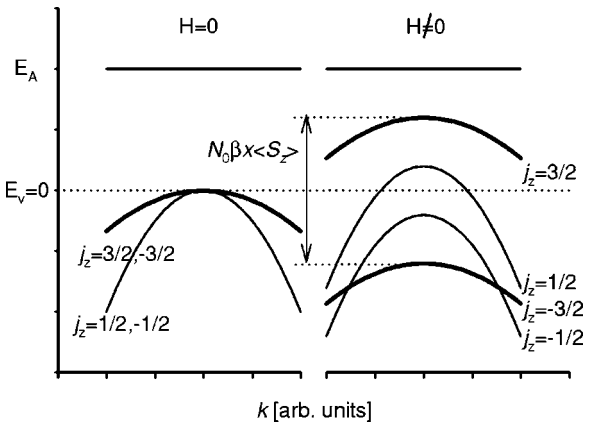

FIG. 1. Band-structure scheme at zero magnetic field (left) and nonzero magnetic field (right) for a *p*-type DMS.

B. Network model

A network model previously introduced for describing electronic transport in disordered semiconductors[36,37] was modified to describe magnetotransport in DMS, i.e., effects due to magnetic-field-induced band splitting and tuning of the disorder potential were included. The basic idea of the network model is to divide the crystal into cubic cells of equal size (characterized by an edge length l) and to assign a local resistance to each cell. The resistances are connected to a network. We use a two-dimensional $N\times N$ square array of cubic cells with index $m\in N^2$ to model the transport in an epitaxial layer. By solving Kirchhoff's equations for the network the macroscopic resistance is derived. The Mn ions are distributed randomly between the cells such that the average of the local Mn concentrations x_m remains x_0. The variation of x_m causes locally different band shifts $E_v^m(j_z,H,T)$ according to Eq. (1) for $k=0$. We add a field-independent contribution,

$$\Delta E_{Dis}^m=m_{Dis}(x_m-x_0), \tag{3}$$

to account for alloy disorder in the valence band. m_{Dis} basically represents the derivative of the average valence-band edge E_V with respect to x at x_0. Thus locally different transport properties, e.g., carrier concentrations arise.

In a calculation of the Fermi level of the entire system the changes of the density of states due to the local band splittings need to be accounted for. This is done by solving the equation for charge neutrality numerically:

$$\sum_{j_z}\sum_{m\in N^2}p_V^{m,j_z}(T)=\sum_{m\in N^2}[n_A^m(T)+n_C^m(T)], \tag{4}$$

where $n_A^m(T)=x_m F^e(E_A,T)$ denotes the local density of ionized acceptors in each cell m. For simplicity, we assume throughout the paper that the Mn ions act as acceptors (like Mn ions in $Ga_{1-x}Mn_xAs$). This is no general limitation of the model. In the case of $Zn_{1-x}Mn_xTe$:N one would replace x_m by a local acceptor density c_m which is independent of x_m. $F^e(E,T)$ is the Fermi function. $n_C^m(T)$ is the number of intrinsic electrons excited via the band gap. For wide-gap DMS's with band gaps $E_G\geqslant 1$ eV and at low temperatures

$T \leqslant 100$ K, it is to a first approximation $n_C^m(T)=0$. $p_V^{m,j_z}(T)$ are the local densities of heavy and light holes of j_z given by

$$p_V^{m,j_z}(T)=\int_{-\infty}^{E_v^m(j_z,H,T)+\Delta E_{Dis}^m} N_{j_z}^m(E)[1-F^e(E,T)]dE, \tag{5}$$

where $N_{j_z}^m(E)$ is the local density of states of the hole band with angular momentum j_z:

$$N_{j_z}^m(E)=\frac{2\pi(2m_{j_z})^{3/2}}{h^3}\sqrt{-[E+E_v^m(j_z,H,T)+\Delta E_{Dis}^m]}. \tag{6}$$

The resistance of an individual cell is given as the parallel resistance of the four hole bands of different j_z. The resistivities $\varrho_{j_z}^m$ of the hole bands of band mobility μ_{j_z} (again, different mobilities μ_{hh} and μ_{lh} are used for heavy and light holes) are given by

$$(\varrho_{j_z}^m)^{-1}=q\mu_{j_z}p_V^{m,j_z}(T), \tag{7}$$

with $p_V^{m,j_z}(T)$ defined in Eq. (5). The cell resistances $R_m=\varrho^m l$ are calculated for each cell. To define the network, we assume the following.

(i) For each cubic cell of the square array, transport can only take place through its four surfaces perpendicular to the plane of the array, i.e., a central cube has four conducting connections with nearest-neighbor cubes.

(ii) The knots of the network are centered in the cells of the array. Thus the resistance $R_{n,m}$ of a conducting connection between two adjacent knots K_m and K_n is $R_{n,m}=\frac{1}{2}(R_n+R_m)$. For every knot K_m of the network it is

$$\sum_{i=1}^{4} I_m^i=0, \tag{8}$$

where I_m^i are incoming and outgoing currents at K_m. Ohm's law relates voltage $U_{n,m}$, current $I_{n,m}$, and resistance $R_{n,m}$ between knots K_n and K_m:

$$U_{n,m}=R_{n,m}I_{n,m}. \tag{9}$$

(iii) The electrodes are modeled by two additional knots on opposite edges of the array. Both electrodes are connected to all N knots of the corresponding edge. One of the electrodes is grounded, i.e., its electric potential is set to zero. To calculate the potential values at the remaining N^2+1 knots (and thus the total resistance R of the array) a system of N^2+1 linear equations needs to be solved employing standard network-analysis algorithms.

For array sizes $N \geqslant 10$ the results obtained for R were independent of the number of cells. Most calculations were performed for arrays with $N=25$ cells and assuming $\mu_{lh} \approx 10\mu_{hh} \approx 1000$ cm^2/V s^2.

C. Mobility model

The model, which we refer to as mobility model, is based on an approach described in a review by Efros and Raikh.[38] Again the model was modified to account for the magnetic-field effects in DMS's. In the network model discussed above, disorder is included via occupation numbers in the different cells leading to different cell resistances which define the total resistance of the network. In this case fluctuations of the electronic potential are averaged on the length scale l of the cells. The model is based on flat bands in each cell and a constant band mobility throughout. The concept of treating the potential fluctuations in the mobility model is entirely different. The locally fluctuating electronic potential of each hole band of the crystal is transformed into a flat potential characterized by a renormalized band edge, i.e., there is no dependence on a scaling length. Instead, in contrast to the network model, an energy-dependent mobility function $\mu_{j_z}(E)$ is introduced, which is determined by the characteristics of the potential fluctuations of the corresponding band:[38]

$$\mu_{j_z}(E)=\frac{q\pi\hbar^4 N}{\sqrt{2}\alpha_{j_z}{}^2 x_0(1-x_0)m_{j_z}^{5/2}\sqrt{E_v(j_z,H,T)+\Gamma_{j_z}-E}}, \tag{10}$$

where N is the number of atoms per unit cell; α_{j_z} is the derivative of the potential with respect to x at x_0, and Γ_{j_z} is the renormalization energy:

$$\alpha_{j_z}=-1/3N_0\beta\langle S_z\rangle j_z+m_{Dis},$$

$$\Gamma_{j_z}=\frac{\alpha_{j_z}{}^2 m_{j_z}x_0(1-x_0)}{2\pi N\hbar^2 a}, \tag{11}$$

where a is the zinc-blende lattice constant. This equation for the mobility is based on a Fermi's-golden-rule description of charge-carrier scattering on fluctuations of a spatially uncorrelated disorder potential that is characterized by a length scale large compared to the lattice constant and comparable with the electron wave length. A parabolic undisturbed dispersion relation for the carriers is assumed. The matrix element appearing in this expression is given by $\langle|V_q|^2\rangle=\alpha x(1-x)/(\Omega N_s)$, where Ω is the volume of the system and N_s the density of scattering centers. The parameter $\alpha=dE/dx|_{x=x_0}$ describes the sensitivity of the carrier energy on fluctuations of the scattering center concentration. The resulting scattering rate is then inserted into an expression of the mobility within the relaxation time approximation, resulting in Eq. (10). From Eq. (10) it can be seen that μ_{j_z} diverges for $\alpha_{j_z}\rightarrow 0$. The equation is only valid when the process determining the mobility is scattering by potential fluctuations. To be able to apply the model in the limit $\alpha_{j_z}\rightarrow 0$, i.e., small potential fluctuations, a mobility limit $\mu_{j_z}^{lim}=\gamma\mu_{lh}$ and $\mu_{j_z}^{lim}=\gamma\mu_{hh}$ for light ($j_z=\pm\frac{1}{2}$) and heavy holes ($j_z=\pm\frac{3}{2}$), respectively, needs to be defined by introducing a cutoff factor γ. μ_{lh} and μ_{hh} are the same band mobilities as

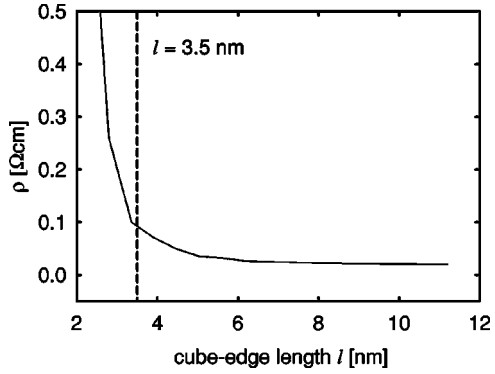

FIG. 2. Resistivity at $H=8$ T of a p-type DMS with $x=0.03$ as a function of cube length l.

for the network model. The mobility limit $\mu_{j_z}^{lim}$ simply reflects a limitation of the mobility by effects other than potential fluctuations, e.g., phonons, etc. The resistivity ϱ_{j_z} of the hole band with angular momentum j_z is given by

$$(\varrho_{j_z})^{-1}=q\int_{-\infty}^{E_v(j_z,H,T)+\Gamma_{j_z}} N_{j_z}\mu_{j_z}(E)[1-F^e(E)]\,dE, \tag{12}$$

where N_{j_z} is the global density of states of the hole band with angular momentum j_z analogous to Eq. (6). To calculate the total resistance R of the crystal the resistances of the four hole bands are connected in parallel again.

III. RESULTS AND DISCUSSION

A. Adjustment of the scaling parameters

Both models contain an adjustable parameter, the edge length l of the cubes in the network model and the factor γ correlating mobility limit and band mobility in the mobility model. These parameters are difficult to define microscopically and are not obviously correlated. We will therefore adjust the parameters such that both models yield comparable zero-field resistances to have the same starting point for the magnetic-field-dependent calculations. The edge length l in the network model defines the volume over which the microscopic alloy disorder is averaged. The larger l is, the smaller are the fluctuations between the x_m. This corresponds to the weighting of disorder effects with respect to occupation effects in the MR. To illustrate this problem, Fig. 2 depicts the resistivity at $H=8$ T of a p-type DMS with $x=0.03$ as a function of cube length l. The fluctuations in the resistivity curve can be considered as a measure for magnitude of the effect of disorder in the network calculation. As expected the fluctuations decrease with increasing l, i.e., disorder effects are averaged out. To assure that disorder effects still play a role, we chose rather arbitrarily $l=3.5$ nm.

The cutoff factor γ in the mobility model is adjusted such that both models yield the same zero-field resistance for the same set of parameters. The procedure is shown in Fig. 3. A good agreement between the two models is obtained for $\gamma=100$.

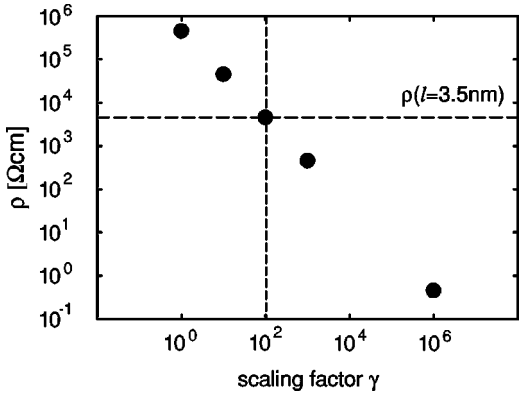

FIG. 3. Zero-field resistivity as a function of cutoff factor γ of the mobility limit in the mobility model calculated for $x=0.03$ at $T=20$ K. The horizontal dashed line represents the value calculated in the network model using $l=3.5$ nm. $T=30$ K, and $E_A=60$ meV.

Before discussing the MR effects calculated using the two models it has to be confirmed that both models exhibit correct temperature characteristics and yield comparable results in zero magnetic field in the entire temperature range. This is done in Fig. 4 which depicts various temperature-dependent resistance curves calculated for different acceptor depth E_A. As expected, typical semiconductor characteristics are derived. For comparison, we also show a curve calculated using the mobility model for $E_A=60$ meV. The two curves calculated with the two models using the same parameters agree very well.

B. Comparison of the models without field-independent disorder

We will now proceed to compare MR curves calculated with the two models for different scenarios. We define the MR value at field H as $[\rho(H)-\rho_0]/\rho_0$ where $\rho(H)$ is the resistivity at field H and ρ_0 is the resistivity at zero magnetic field. We always assume in this Sec. III B that there is no Mn-related disorder at zero magnetic field, i.e., the disorder parameter $m_{dis}=0$ meV. Figures 5 and 6 show MR curves calculated for various x ranging from 0.005 to 0.03 using the

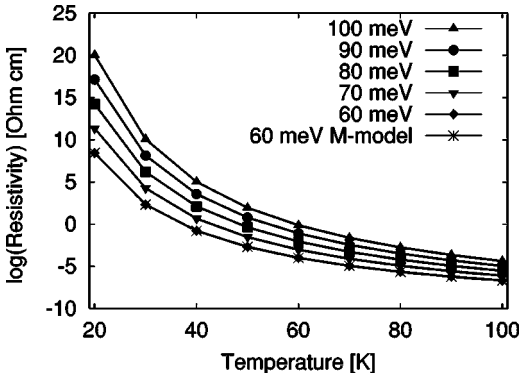

FIG. 4. Temperature dependence of the resistance calculated using the network model (various acceptor depths) and using the mobility model ($E_A=60$ meV only).

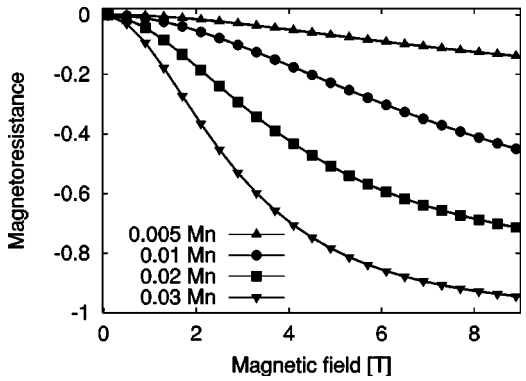

FIG. 5. Magnetoresistance for various x calculated using the network model. $T=40$ K, $E_A=60$ meV.

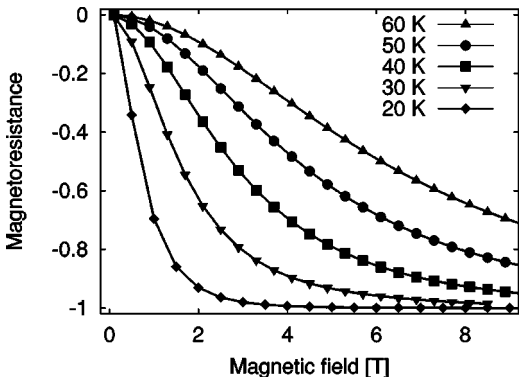

FIG. 7. Magnetoresistance for various T calculated using the network model. $x=0.03$, $E_A=60$ meV.

network model and the mobility model, respectively. The temperature was fixed to $T=40$ K and the acceptor energy was $E_A=60$ meV. Distinct differences between the two models occur. The network model only exhibits negative MR effects for all x with the MR decreasing in the entire field range. A small plateau at very low fields is followed by a rapid decrease at intermediate fields before saturating at higher fields. The larger the Mn concentration x, the more pronounced is the resulting MR effect. The actual shape of the MR curve does not vary significantly with x.

The situation is very different for the MR curves shown in Fig. 6 calculated using the mobility model. In this case the MR effect changes its character with increasing field, a decrease is followed by an increase giving rise to a minimum in the MR curve. However, the increase becomes weaker and finally the MR decreases again at very high fields causing a maximum. With decreasing Mn concentration x, the minimum and the maximum both shift to higher fields. For $x=0.01$ and $x=0.005$ the maximum occurs at $H=10$ T and $H\approx 20$ T, respectively. Furthermore, the minimum becomes shallower and the positive MR contribution is enhanced causing the maximum to be more pronounced.

Figures 7 and 8 demonstrate the effect of temperature on the MR curves calculated using the two models. The Mn concentration as well as the acceptor depth are kept constant at $x=0.03$ and $E_A=60$ meV, respectively. In the case of the network model, the MR curves are negative at all temperatures and basically of the same shape, i.e., a small plateau at very low fields is followed by a rapid decrease at intermediate fields before saturating at higher fields. As expected, the saturation value is the same for all T. The curves show a scaling behavior, the higher the temperature T, the higher the field value H to reach the same MR value.

Again, the situation is very different for the MR curves at different temperatures calculated using the mobility model compared to those derived with the network model. At all temperatures the MR curves also saturate at the same negative MR value at very high fields H, but, in contrast to the network model, there is no obvious scaling behavior. This can be seen directly in Fig. 8, for the curves at $T=20$ K and 30 K, and was confirmed for the higher temperatures in calculations up to $H=20$ T. As already discussed in Fig. 6, there is a negative as well as a positive contribution to the MR which are of the same order of magnitude. At the lowest temperature shown, $T=20$ K, the positive contribution is very small and the MR curve is dominated by the negative MR effect and strongly resembles the corresponding MR curve in Fig. 7. Even the MR value at saturation, the saturation field and the curve shape are comparable. As the positive MR contribution in the mobility model becomes more significant with increasing T, the two models start to differ considerably.

The observed MR behavior in both models is related to the interplay of magnetic-field-induced disorder effects and

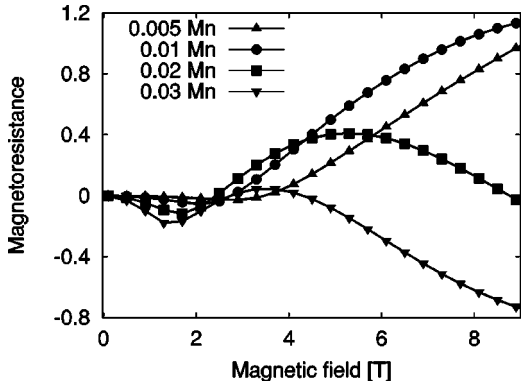

FIG. 6. Magnetoresistance for various x calculated using the mobility model. $T=40$ K, $E_A=60$ meV.

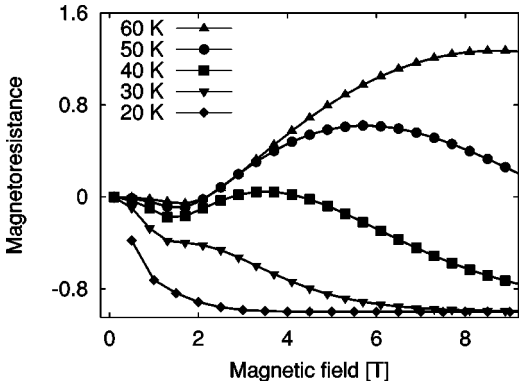

FIG. 8. Magnetoresistance for various T calculated using the mobility model. $x=0.03$, $E_A=60$ meV.

occupation effects. Two types of occupation effects arising due to the giant Zeeman splitting can be imagined: (i) the magnetic-field-induced band shifts of the individual bands change the number of holes within each band; and (ii) the magnetic-field-induced band splitting of the four hole bands changes the total density of states of the valence band as a function of energy. The differences between the two models mainly arise due to a different weighting of the various effects.

Let us first consider the results of the network model. Disorder effects and both types of occupation effects are responsible for the observed plateau in the MR curves at low fields in Figs. 5 and 7. The resulting deviation from the ''Brillouin behavior'' of the MR is particularly obvious at low x and high T. At zero field, light and heavy holes are degenerate. The transport is determined by the two light hole bands because $\mu_{lh} \approx 10\mu_{hh}$. Applying a small magnetic field has several effects, it splits the hole bands and the resulting changes of the density of states cause different occupations of the two light hole bands (similar for the two heavy hole bands), i.e., one contributes more to the transport, the other one less. At low fields, these two contributions to a first approximation cancel out, i.e., the resistance of the individual cell does hardly depend on field. Furthermore, in the regime without field-independent disorder discussed here, all the cells have exactly the same resistance in zero field. Thus in zero field, the geometrically shortest current path through network has the lowest resistance. This changes when a magnetic field is applied as the field-induced disorder randomly modifies the resistances of the cells leading to percolation effects, i.e., in general, the current path with the lowest resistance is longer than the geometrically shortest path. Thus, the disorder effect results in an additional positive MR contribution at low fields. The sum of these effects causes the observed plateau in the MR curves.

When increasing the field further the energy splitting becomes such that only the light hole and the heavy band closest to the acceptor level contribute to the transport. In this field regime the transition from light hole to heavy hole dominated transport takes place, i.e., occupation effects cancel out the difference in mobility between the two bands. At even higher fields the MR curves derived with the network model are entirely dominated by occupation effects of the first type. The highest heavy-hole band with $j_z = \frac{3}{2}$ rapidly approaches the acceptor level and its occupation increases almost exponentially. Therefore, the $j_z = \frac{3}{2}$ band has the lowest local resistance in each cell (i.e., at each knot), as can be seen from Eqs. (5) and (7), and carries the current. As this is the case for each cell, the transport is determined by this band alone whereas the other three bands hardly contribute. As a consequence the strong negative MR effect arises. The curve shape of the MR basically follows a Brillouin function [see Eq. (2)] which determines the energetic shift of the $j_z = \frac{3}{2}$ heavy-hole band towards the acceptor according to Eq. (1).

This explains the observed behavior as a function of Mn concentration x in Fig. 5 and of temperature T in Fig. 7 at all fields. The behavior of plateau with x and T simply reflects the behavior of the magnetic-field value where the transition from multiband transport to single-band transport takes place. At high fields, with increasing Mn content the saturation value of the giant Zeeman splitting $\frac{5}{2}N_0\beta x$ increases causing larger negative MR effects at saturation. With increasing T the magnetic-field value required to overcome the thermal disorder of the system of Mn spins increases. Hence, the Brillouin function saturates at a higher field, but the corresponding saturation value of the giant Zeeman splitting is independent of T. This is reflected by the corresponding MR curves, i.e., by their scaling behavior and saturation values.

We will turn now to the discussion of the MR curves calculated using the mobility model (Figs. 6 and 8). The main difference between the two models is the strong positive MR contribution at intermediate fields in the mobility model, which becomes very pronounced with increasing T and decreasing x. It is a result of a stronger weighting of magnetic-field-induced disorder effects in the mobility model than in the network model. For each hole band, the disorder is included in the model via two parameters, the disorder parameter α_{j_z} and the band renormalization Γ_{j_z}.

Before discussing the MR curves in detail, we address the field dependence of these two parameters. From Eq. (10), it can be seen that the energy-dependent mobility $\mu_{j_z}(E)$ is inversely proportional to the square of α_{j_z} defined by Eq. (11). In zero field, α_{j_z} is zero for all j_z because we exclude field-independent disorder, i.e., $m_{Dis}=0$, and the average Mn-spin alignment $\langle S_z \rangle = 0$. At low fields, the Brillouin function is proportional to the magnetic field, hence, $\alpha_{j_z} \propto \langle S_z \rangle \propto H$ and consequently $\mu_{j_z} \propto H^{-2}$ for all bands. The mobility of all four hole bands decreases dramatically when the magnetic field is applied and saturates at the field where the Brillouin function saturates, i.e., $\langle S_z \rangle = -\frac{5}{2}$. Following the above arguments, one finds that the band renormalization $\Gamma_{j_z} \propto H^2$ at low fields and that it also saturates at higher fields. It is important to note that Γ_{j_z} is positive for all j_z, i.e., causing an additional shift of all four hole bands towards the acceptor with increasing field. In particular, for the hole bands with $j_z = -\frac{3}{2}$ and $j_z = -\frac{1}{2}$ the band renormalization Γ_{j_z} counteracts the shifts due to the giant Zeeman splitting. The disorder-induced renormalization of the band gap enhances the occupation of all four bands. This effect dominates at low fields leading to the local minimum in the MR curve. At intermediate fields, the field-induced drop of the mobility becomes the dominant effect and causes the positive MR contribution leading to the maximum in the MR curve. In the low and intermediate field regimes, as in the network model, all bands contribute to the transport. At very high fields and low temperatures the transport is dominated by the heavy-hole band with $j_z = \frac{3}{2}$ as discussed above. The observed x and T dependence of the positive MR contribution and the corresponding maximum in the MR curves reflect its origin as a disorder effect. In contrast, to occupation effects, which become less relevant with increasing temperature or decreasing band splitting effects ($\propto x$), the disorder-induced drop of the mobility is always of the same relevance. The shift of the maximum to higher temperatures reflects again the dependence of the changes of $\mu_{j_z}(E)$ on $\langle S_z \rangle$.

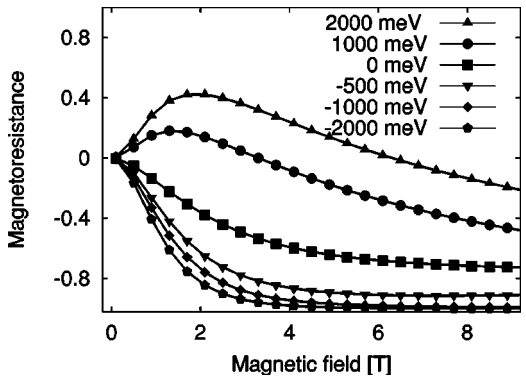

FIG. 9. Magnetoresistance for various disorder parameters m_{Dis} calculated using the network model. $T=20$ K, $E_A=60$ meV, $x=0.01$.

C. Comparison of the models including field-independent disorder

We will now focus on the aspect of magnetic-field independent disorder. In our approach, we solely consider alloy disorder in the valence band represented by m_{Dis} in Eqs. (3) and (11). m_{Dis} is simply the derivative of the valence-band edge with respect to Mn concentration at x_0. As in Sec. III B the electronic potential in zero field is the same for all holes, independent of j_z. One should note, however, that there is a strong correlation between alloy potential fluctuations and local magnetic-field splitting as both variables depend linearly on x.

It is useful to first consider the limit of large $|m_{Dis}|$, i.e., when the alloy disorder is bigger than the p-d induced band splitting at saturation: With increasing magnetic field and for positive m_{Dis}, the disorder increases for the hole bands approaching the acceptor and decreases for the hole bands moving away from the acceptor. This means qualitatively that the mobility decreases with increasing field for the bands whose occupation increases with the field, i.e., the MR contributions of disorder effects and occupation effects are of opposite sign. The situation is vice versa for negative m_{Dis}.

In the network model where constant, field-independent band mobilities are assigned to the hole bands a ''decrease in mobility'' with increasing disorder is caused by percolation

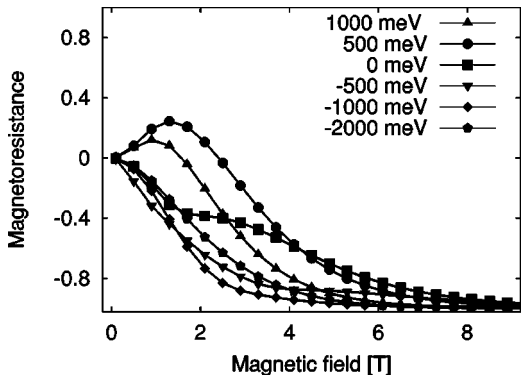

FIG. 10. Magnetoresistance for various disorder parameters m_{dis} calculated using the mobility model. $T=20$ K, $E_A=60$ meV, $x=0.01$.

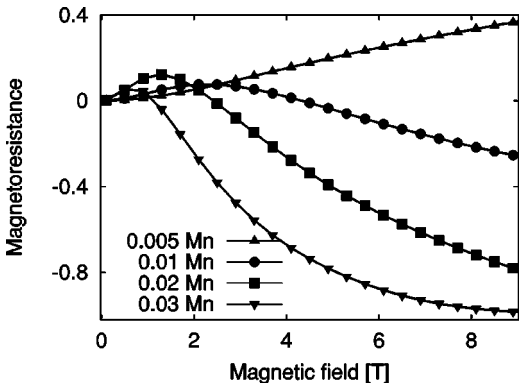

FIG. 11. Magnetoresistance for various x calculated using the network model. $T=30$ K, $E_A=60$ meV, $m_{Dis}=1000$ meV.

effects, i.e., an elongation of the current path of lowest resistance through the network. In the mobility model, the effect is more obvious increasing α_{j_z} simply decreases $\mu_{j_z}(E)$ according to Eq. (10).

Figures 9 and 10 show MR curves calculated with the network and mobility model, respectively, in the limit of large $|m_{Dis}|$. Different values of m_{Dis} were used. A calculation for $m_{Dis}=0$ meV is shown for comparison. The other parameters were $x=0.01$, $E_A=60$ meV, and $T=20$ K. Both sets of MR curves show the behavior discussed above and now qualitatively yield similar results. Large positive m_{Dis} values yield MR curves showing a positive effect and a characteristic maximum. Large negative m_{Dis} values yield MR effects in the entire field range with a saturation at the highest fields. As already vaguely indicated by the results in Sec. III B, positive MR contributions as well as changes of shape of the MR curve seem to be more pronounced for the same m_{Dis} value in the mobility model compared to the network model. This reflects again the different weighting of occupation and disorder effects in the two models.

The good agreement of the MR behavior calculated using the two models in this case is further confirmed by the derived MR curves for different Mn concentrations x in the presence of field-independent disorder. The results displayed in Figs. 11 and 12 are calculated for various x between 0.005 and 0.03 and for $m_{Dis}=1000$ meV using the parameters $T=30$ K and $E_A=60$ meV. As expected, the positive MR effects are more pronounced at low x reflecting that the band

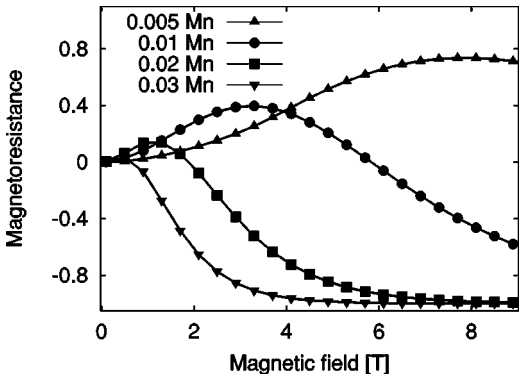

FIG. 12. Magnetoresistance for various x calculated using the mobility model. $T=30$ K, $E_A=60$ meV, $m_{Dis}=1000$ meV.

splittings decrease for smaller x and hence occupation effects become less important. Again, the magnitude of the effects as well as the obtained curve shapes even show a quantitative agreement.

IV. CONCLUSIONS

The network model and the mobility model for the hole transport in p-type DMS both yield positive as well as negative MR effects even in the absence of hole-hole and hole-acceptor interactions. Whether the derived MR effect is positive or negative depends entirely on the subtle interplay of disorder effects (comprising field-independent disorder and magnetic-field-induced disorder) and occupation effects (due to the magnetic-field-induced band-structure changes). Both models contain an adjustable parameter, the edge length l of the cubes of in the network model and the factor γ correlating the mobility limits and the band mobilities in the mobility model, which are hard to define microscopically and are not obviously correlated. Nevertheless, when adjusting the parameters such that both models yield comparable zero-field resistances, the MR curves calculated with the two models are in qualitative and even quantitative agreement for a wide range of parameters. Furthermore, the two models are in excellent qualitative agreement with recent experimental results on p-type $Zn_{1-x}Mn_xTe$:N and $Ga_{1-x}Mn_xAs$ in the paramagnetic phase.

ACKNOWLEDGMENTS

We thank H. Overhof for fruitful discussions concerning the network model and B. Goldlücke for his help with the numerical algorithms. One of us (S.D.B.) is grateful for support by the Fonds der Chemischen Industrie.

*Electronic address: klarp@mailer.uni-marburg.de

[1] H. Ohno, F. Matsukura, and Y. Ohno, Solid State Commun. **119**, 281 (2001).
[2] O. Goede and W. Heimbrodt, Phys. Status Solidi B **146**, 11 (1988).
[3] J.K. Furdyna, J. Appl. Phys. **64**, R29 (1988).
[4] G.A. Prinz, Science **250**, 1092 (1990).
[5] A.M. Nazmul, S. Sugahara, and M. Tanaka, Phys. Rev. B **67**, 241308 (2003).
[6] T. Dietl, H. Ohno, F. Matsukura, J. Cibert, and D. Ferrand, Science **287**, 1019 (2000).
[7] T. Jungwirth, J. König, J. Sinova, J. Kucera, and A.H. MacDonald, Phys. Rev. B **66**, 012402 (2002).
[8] D. Ferrand, J. Cibert, A. Wasiela, C. Bourgognon, S. Tatarenko, G. Fishman, T. Andrearczyk, J. Jaroszynski, S. Kolesnik, T. Dietl, B. Barbara, and D. Dufeu, Phys. Rev. B **63**, 085201 (2000).
[9] B.T. Jonker, Y.D. Park, B.R. Bennett, H.D. Cheong, G. Kioseoglou, and A. Petrou, Phys. Rev. B **62**, 8180 (2000).
[10] R. Fiederling, M. Keim, G. Reuscher, W. Ossau, G. Schmidt, A. Waag, and L.W. Molenkamp, Nature (London) **402**, 787 (1999).
[11] M. Oestreich, J. Hübner, D. Hägele, P.J. Klar, W. Heimbrodt, W.W. Rühle, D.E. Ashenford, and B. Lunn, Appl. Phys. Lett. **74**, 1251 (1999).
[12] G. Schmidt, G. Richter, P. Grabs, C. Gould, D. Ferrand, and L.W. Molenkamp, Phys. Rev. Lett. **87**, 227203 (2001).
[13] M. Tanaka, Semicond. Sci. Technol. **17**, 327 (2002).
[14] P.J. Wellmann, J.M. Garcia, J.L. Feng, and P.M. Petroff, Appl. Phys. Lett. **73**, 3291 (1998).
[15] S. Ye, P.J. Klar, Th. Hartmann, W. Heimbrodt, M. Lampalzer, S. Nau, T. Torunski, W. Stolz, T. Kurz, H.-A. Krug von Nidda, and A. Loidl, Appl. Phys. Lett. **83**, 3927 (2003).
[16] H. Akinaga, J. De Boeck, G. Borghs, S. Miyanishi, A. Asamitsu, W. Van Roy, Y. Tomioka, and L.H. Kuo, Appl. Phys. Lett. **72**, 3368 (1998).
[17] D.R. Schmidt, A.G. Petukhov, M. Foygel, J.P. Ibbetson, and S.J. Allen, Phys. Rev. Lett. **82**, 823 (1999).
[18] M. Mizuguchi, H. Akinaga, K. Ono, and M. Oshima, J. Appl. Phys. **87**, 5639 (2000).
[19] H. Akinaga, S. Miyanishi, K. Tanaka, W. Van Roy, and K. Onodera, Appl. Phys. Lett. **76**, 97 (2000).
[20] Y.D. Park, A. Wilson, A.T. Hanbicki, J.E. Mattson, T. Ambrose, G. Spanos, and B.T. Jonker, Appl. Phys. Lett. **78**, 2739 (2001).
[21] Y. Shapira, N.F. Oliveira, Jr., P. Becla, and T.Q. Vu, Phys. Rev. B **41**, 5931 (1990).
[22] Y. Shapira, N.F. Oliveira, Jr., D.H. Ridgley, R. Kershaw, K. Dwight, and A. Wold, Phys. Rev. B **34**, 4187 (1986).
[23] Y. Shapira, D.H. Ridgley, K. Dwight, A. Wold, K.P. Martin, and J.S. Brooks, J. Appl. Phys. **57**, 3210 (1985).
[24] K.-T. Nam, N. Watanabe, S. Kuroda, and K. Takita, J. Supercond. **16**, 335 (2003).
[25] S. Ye, P.J. Klar, T. Henning, M. Lampalzer, W. Stolz, and W. Heimbrodt, J. Supercond. **16**, 159 (2003).
[26] C. Haas, Phys. Rev. **168**, 531 (1968).
[27] M. Sawicki, T. Dietl, J. Kossut, J. Igalson, T. Wojtowicz, and W. Plesiewicz, Phys. Rev. Lett. **56**, 508 (1986).
[28] J. Stankiewicz, S. von Molnar, and W. Giriat, Phys. Rev. B **33**, 3573 (1986).
[29] Y. Ono and J. Kossut, J. Phys. Soc. Jpn. **53**, 1128 (1984).
[30] T. Wojtowicz, T. Dietl, M. Sawicki, W. Plesiewicz, and J. Jaroszynski, Phys. Rev. Lett. **56**, 2419 (1986).
[31] T. Dietl, J. Antoszewski, and L. Swierkowski, Physica B & C **117&118**, 491 (1983).
[32] H. Falk, P.J. Klar, and W. Heimbrodt, Thin Solid Films **380**, 215 (2000).
[33] P.J. Klar, H. Falk, and W. Heimbrodt, Solid State Commun. **116**, 125 (2000).
[34] S.M. Ryabchenko, Yu.G. Semenov, and O.V. Terletskii, Sov. Phys. Solid State **27**, 1746 (1985).
[35] S.A. Crooker, D.G. Rickel, S.K. Lyo, N. Samarth, and D.D. Awschalom, Phys. Rev. B **60**, R2173 (1999).
[36] H. Overhof and P. Thomas, *Electronic Transport in Hydrogenated Amorphous Semiconductors*, Springer Tracts in Modern Physics Vol. 114 (Springer, Berlin, 1989).
[37] H. Overhof, M. Otte, M. Schmidtke, U. Backhausen, and R. Carius, J. Non-Cryst. Solids **230**, 992 (1998).
[38] A.I. Efros and M.E. Raikh, *Effect of Composition Disorder on the Electronic Properties of Semiconducting Mixed Crystals*, in *Optical Properties of Mixed Crystals*, edited by R.J. Elliott and I.P. Ipatova (Elsevier, New York, 1988).